# A Physics-Based Power Model for Skid-Steered Wheeled Mobile Robots

Sedat Dogru and Lino Marques, *Member, IEEE*

*Abstract*—The power consumed by skid-steered mobile robots varies enormously depending on their operating regimes and environments. Therefore, energy optimal planning of field missions can be accomplished only if the operating environment and an accurate model of the robot's power consumption are known in advance. This paper studies influences of location of the center of mass, surface type, terrain relief, platform geometry, radius of curvature, speed, and temperature on the power consumption of a skid-steered mobile platform and derives a physics-based power model that uses friction to accurately model the power consumed for the most relevant parameters inside a wide range of operating conditions. This paper also shows how friction can be measured using power consumed by the motors and how motor constants can be measured in a noninvasive end-to-end manner. Our findings were validated with a Clearpath's Husky A200 platform, driving it indoors and outdoors on different surfaces, varying the speed, the radius of curvature, the mass, and the center of mass location, resulting in a dense dataset on which the derived model as well as the temperature dependence of the power consumption was verified.

*Index Terms*—Field robotics, friction estimation, mobile robots, power characterization, skid steer, terrain, unmanned ground vehicle (UGV).

## I. INTRODUCTION

SKID-STEERED mobile robots are simple, robust, highly maneuverable, and compact [1]–[3], and therefore are very useful for certain applications, such as farming, excavation, demining, and military. Skid-steered vehicles have high traction since all their wheels are directly coupled to one of the motors, making them better suited for rough terrains. They have a zero radius of curvature, making them quick and easily maneuverable, which is advantageous for military applications, and also for civil applications where space for a large turning radii is not available. They behave like differential drive vehicles and do not use any explicit steering mechanism and, therefore, path planning and even control approaches from differential wheeled robots can be used with minimal modifications. The absence of

a steering mechanism, in contrast to, for example, Ackermann steered vehicles, voids the need for a space for the steering mechanism, resulting in a compact system.

Skid-steered vehicles are driven by changing the velocities of the right and left wheels or tracks independently. When wheels on both sides are rotating at the same speed, the vehicle moves straight ahead. As soon as wheels of one side become slower, the vehicle is forced to rotate around an axis, which is outside the wheels of the vehicle. The rotational axis is usually not perpendicular to any of the wheels, causing skid and increasing the vehicle's energy consumption. The amount of skid depends on the radius of curvature, i.e., the speed difference between the left- and right-side wheels or tracks, and increases with decreasing radius of curvature. The amount of energy lost due to skid depends a lot on the surface and the maneuvers. It is not surprising to see orders of magnitude difference between skid and pure translational motion. For example, in our tests on a wood tiled floor, the average power consumed by the robot as the wheels of both sides moved at approximately 0.1 m/s forward was 18 W. However, when wheels rotated at the same speed but in opposite directions, the measured power consumption was 212 W. As this sample measurement strongly suggests, for energy efficient operation of skid-steered vehicles, their motion on a given terrain should be properly planned based on *a priori* characterization of their power consumption.

Proper power consumption characterization is useful in mission planning, mission cost estimation and range prediction [4]–[8], sensor scheduling [9], [10], cheaper exploration [11], generation of cheaper paths and trajectories [12]–[17], autonomous operation, and even vehicle design. For example, a 10-fold increase in the power consumption of an electric motor powered platform also means at least $\sqrt{10}$-fold increase in the torques the motor should provide, and a corresponding increase in the strength and rigidity the drive mechanism as well as the structure should have. The need for this characterization has led to some work in the literature, with studies both on tracked [18]–[21] and on wheeled vehicles [22], [23].

One of the major limitations of these studies is that most of them do not investigate the whole motion range of the vehicle, leading to models that work only in a subset of the operating range. This subset is sometimes even restricted to just straight motion. The proposed mathematical models are not intuitive and are sometimes restricted to just curve fitting. Studies using friction for characterization ignore variance of friction with speed and with the radius of curvature. Our field measurements showed that both the speed as well as the radius of curvature

This article has been accepted for inclusion in a future issue of this journal. Content is final as presented, with the exception of pagination.

2

IEEE TRANSACTIONS ON ROBOTICS

affect the friction. And yet some of these studies do not pay attention to terrain relief and terrain type, and model the power as a function of speeds only for flat surfaces, which voids the model on rough fields, which are the most common in real applications. Although some studies take into account the instantaneous center of rotation (ICR) for power characterization, they fail to take into account the vehicle geometry. Skid of two skid-steered vehicles differing only by size but doing the same maneuver are expected to be different, the longer one skidding more, and as a result consuming more power.

The main contribution of this paper is an accurate and comprehensive model for power consumption in skid-steered platforms. The model takes into account the power consumption of a skid-steered wheeled robot along its whole motion range, taking into consideration terrain relief. This characterization is based on the friction between the robot and the surface, and it is measured using a black-box model, which does not have access to any current or torque measurements on the motors, but has access to the power fed to the motor controllers, wheel velocities as well as pitch and roll measurements of the platform. The model also takes into account the rise in the temperature of the motors which may increase the error in the estimated friction, preventing its use for different temperatures of the system. Rise in the temperature of the motors will result in extra losses as well, increasing the total power consumption, and this is ignored in the literature. The location of the center of mass of the robot, which does not have to be at its geometric center, is also taken into account. The proposed model allows both to qualitatively understand how friction changes with the size of the robot, as well as its center of mass, and it also allows friction estimates obtained in a given center of mass configuration be used with a different one. The proposed model, being based on friction, allows generalized power consumption estimation irrespective of the weight of the platform or relief of the surface.

The proposed model is based on assuming that a skidding wheel is subject to both rolling and skidding frictions, which act independently. Skid in a skid-steered platform is initiated by a finite radius of curvature (nonstraight motion), which forces the wheels to move along a circle. However, usually none of the wheels are perpendicular to the line connecting them to the ICR, making an angle known as the slip angle. This angle divides the net resultant force acting on the wheel into two components, one parallel to the wheel, forcing it to rotate, and the other perpendicular, causing it to skid. As it is clear from this reasoning, the amount of skid is determined by the slip angle, which means larger slip angles, i.e., smaller radius of curvatures, and more skid, resulting in more friction. Since a skid-steered vehicle has two sides, lets call them inner (passive) and outer (active), skid will be experienced by both sides, and the net friction will depend on slip angles of all the wheels.

Our field measurements show that skid friction depends on the translational speed of the robot, requiring a different model fit for different speeds. Dependence of skid friction on velocity is actually expected, in the light of research on rubber friction [24], [25]. Friction coefficient of rubber sliding over a hard surface has roughly a bell shape. It starts with small values at very slow speeds ($10^{-7}$ m/s) reaching maximum at low speeds and then decreases for higher speeds. The speed where maximum friction is measured as well as the shape of the curve varies with the surface, rubber composition, and the temperature.

The following section provides a detailed review of related work, followed by a section on the mathematical models used to estimate friction and the model of effective friction during skid motion. Section IV describes the test environment and Section V provides a detailed presentation and discussion of the experimental measurements as well as error analysis showing that the proposed model fits the experimental measurements with high accuracy. Section VI summarizes the main conclusions of this paper.

## II. RELATED WORK

This section describes some works on energy efficient operation of mobile robots, then details where power consumption characterization is useful, followed by a detailed list of works done on power consumption characterization of skid-steered robots.

Energy efficient operation of mobile robots can be achieved in various ways. Mei *et al.* [9] found experimentally that in a differentially driven Pioneer 3DX robot, the sensors, the microcontroller, and the embedded computer use up to 65% of the total power consumed by the robot. They also showed that marginal power savings can be achieved by reducing the scanning frequency of the sonar array. Brateman *et al.* [10] showed that by scheduling motor speed and processor frequency while preventing collisions can contribute to energy savings. Their approach was justified by the fact that stereo image operations are processor intensive, and by adapting the frequency of these operations to the speed of the robot will contribute to the overall efficiency. Ooi *et al.* [12] studied path optimization in a scenario where the robot is required to relay high amounts of data through one or more base-stations, taking into account the power consumption of wireless communication. Mei *et al.* [11] improved energy efficiency of exploration by taking into account the power spent in rotations as a path is planned for the next frontier cell. Using Dijkstra's algorithm, they also showed that longer paths with less rotations can be more energy efficient. Sun *et al.* [13] take into account friction and gravity in finding energy efficient paths across a terrain.

Some works concentrate more on the control aspects to improve energy efficiency. Duleba and Sasiadek [26] used a modified version of Newton's algorithm to generate energy efficient motion plans for a unicycle robot, with smooth and easy to generate motor control references. Kim and Kim [27] showed theoretically that energy efficiency of translational motion for wheeled mobile robots can be improved by varying the velocity profile of the motor, where instead of applying constant acceleration and deceleration, variable acceleration and deceleration are applied as the robot starts to move or stop. In this way, an improvement of up to 30% in efficiency was achieved. Broderick *et al.* [14] described a cost function that takes into account time and energy efficiency to generate trajectories, i.e., velocity controls, for coverage patterns created by path planning. Sadrpour *et al.* [28] studied a teleoperated unmanned ground vehicle

This article has been accepted for inclusion in a future issue of this journal. Content is final as presented, with the exception of pagination.

DOGRU AND MARQUES: PHYSICS-BASED POWER MODEL FOR SKID-STEERED WHEELED MOBILE ROBOTS 3

(UGV), instead of an autonomous one, and showed that the driving style of the operator may affect the energy consumption of the UGV.

Energy characterization is also important to estimate the energy remaining in the battery. Berenz *et al.* [4] compared the risk of running out of battery to the gain from being operational. As a result of their tests both in simulation and on cleaning robots, they showed that some increase in risk may result in a meaningful increase in mission duration, but up to some point. Sadrpour *et al.* [5] described two different methods to predict the energy requirements for a UGV mission. Those methods are a linear regression model that uses the current velocity and power consumption, and a Bayesian regression model that also takes into account prior knowledge, which was later experimentally validated in [6]. Parasuraman *et al.* [7] discussed a generic approach to predict the energy requirements for a mission based on predetermined power models of a robot. Broderick *et al.* [8] discussed usage of hybrid power sources for a UGV. Their power sources were a normal battery and a fuel cell, which provides constant current, but needs considerable time to start-up and shutdown, consuming energy in these stages.

Various power consumption models have been used in the literature. Linear power consumption models have given satisfactory results for differential wheel drive robots [9], [29], such as Pioneer 3DX, where they have a fixed offset and a constant factor multiplied by the motor speed. However, those linear models are not applicable to skid steer robots. Linear models are used only with partial success, when explaining energy consumption of pure translational motion. As soon as rotations enter the picture, the linearities are lost.

Although the detailed interactions between the wheels and the terrain are complex in general, the cumulative behavior is relatively simpler, allowing conclusions to be made about the amount of friction or power consumption. Guo and Peng [18] proposed a simple second-order velocity only model for the power consumption of a tracked vehicle, an iRobot Packbot, on sand. Their model did not take into account the electrical subsystem, and their work did not consider the full motion range of the robot, leading to a model that can properly estimate power consumption only during translations. Yu *et al.* [22] studied a skid-steered wheeled robot, a modified Pioneer 3-AT, proposing a motion supporting and a motion opposing friction coefficient in addition to the rolling friction coefficient, all invariant of the speed or the radius of curvature of the robot. The coefficients are used in conjunction with shear displacement to estimate power consumption. Broderick *et al.* [19] concentrated on measuring energy consumption of a tracked robot, a Packbot, mainly along straight lines running at different speeds, which was done by experimentally measuring power consumption along straight lines and rectangles with large circular corners on grass or asphalt. Morales *et al.* characterized the power consumption of a tracked robot [20], as well as a wheeled skid-steered robot [30]. The models used to estimate power consumption due to skid were based on the ICR, as well as the pressure under each contact point, which was experimentally measured for the wheeled robot [30], as well as a linear combination of the speeds of each side. Chuy *et al.* [23] modeled the power consumption of a

skid-steered robot using an exponential with an offset. Pentzer *et al.* [21] used an extended Kalman filter to estimate location of the ICR, and a recursive least square algorithm to learn terrain-related power model parameters for a skid-steered wheeled mobile robot. This way they were able to estimate power usage of a skid-steered wheeled mobile robot. The work described in this paper advances the previous studies by a model that works across the whole motion range of the robot, like our recent previous work [31], and it extends this previous work by taking into account different center of mass locations, as well as studying temperature effects and showing how motor parameters can be measured.

## III. MATHEMATICAL MODEL

We first discuss how the friction coefficient can be calculated from the power measurements of a robot driven by dc motors, taking into account terrain relief. Although in this section, we assume the model of a brushed dc motor, which is the type of motor used on our robot (Husky A200), this discussion is valid for other types of electric motors employed in mobile robots' power trains, namely brushless dc motors (BLDC). This is justified by the fact that the input power of all types of dc motors is the mechanical power they deliver, which is torque times speed, plus copper losses, which are proportional to the square of the current and this current is proportional to the torque delivered. Friction calculation in this section is followed by a study of temperature effects on the power consumption and friction estimation; then, the motion of skid-steered robot is classified and a proper mathematical model on the friction arising during skid is presented.

### A. Friction Estimation

The power consumed by a dc motor is given by

$$P_{\text{IN}} = I_a^2 R_a + I_a E_b \tag{1}$$

where $I_a$ and $R_a$ are the armature current and resistance, respectively, $E_b$ is the back electromotive force (EMF) of the motor, and $P_{\text{IN}}$ is the power input to the motor. $I_a^2 R_a$ corresponds to the copper losses on the motor, and $I_a E_b$ corresponds to the mechanical power output of the motor.

The mechanical outputs of a dc motor are torque $T$ and rotational speed of the shaft $\omega_{\text{shaft}}$, which are proportional to the armature current $I_a$ and the back EMF $E_b$. Note that the torque and speed output of the motor are proportional to the force applied by the wheels $F_{\text{wheels}}$ and their speed $w$, respectively. This results in the following power equation for a dc motor

$$P_{\text{IN}} = k_1 F_{\text{wheels}}^2 + k_2 \omega F_{\text{wheels}} \tag{2}$$

where $k_1$ and $k_2$ are proportionality constants summarizing the torque constant, armature resistance, wheel radius, and efficiency.

Note that if the power is measured not at the motors but at their controllers, the measured losses will increase. Losses in a dc motor controller are mainly due to the internal resistances of the MOSFETs in the power bridge circuit [32], and as a result they are proportional to the square of the current. Therefore, if
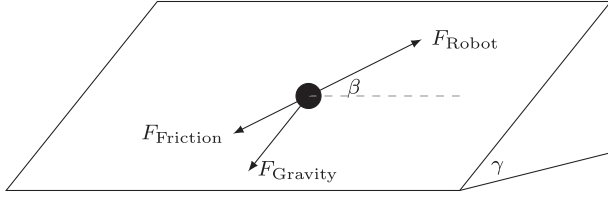
Fig. 1.    Angles used and the forces acting on the robot on a terrain with relief.

the powers are measured at the controller, instead of the motor, the first term of (1) corresponding to the losses can be updated to $I_a^2 R_a'$, where $R_a'$ is the equivalent resistance of the armature and the MOSFETs.

A robot moving on an inclined plane will be subject to gravity as well as friction along its axis of motion. When it climbs, it has to overcome gravity, as well as friction. When it descends, depending on the relative size of gravitational pull and friction, the robot will spend energy either to help gravity overcome friction, or to oppose gravity to keep constant speed. Therefore, the magnitude of the force required by the robot as it moves uphill or downhill, and provided by the wheels, is

$$F_{\text{up/down}} = |F_{\text{gravity}} \pm F_{\text{friction}}| \qquad (3)$$

where the force acting on the robot due to gravity and the force due to friction are, respectively, given by

$$F_{\text{gravity}} = mg \sin\gamma \sin\beta \qquad (4)$$

$$F_{\text{friction}} = \mu mg \cos\gamma \qquad (5)$$

where $\gamma$ is the local inclination angle of the point where the robot is, and $\beta$ is the angle between the horizontal direction and the heading direction of the robot (see Fig. 1), and $\mu$ is the friction coefficient.

Using (2)–(5) and $F_{\text{wheels}} = F_{\text{up/down}}$, we get the following second-order equation in terms of the friction coefficient for arbitrary terrain

$$\begin{aligned} P_{\text{IN}} = {}& \mu^2 k_1 m^2 g^2 \cos^2\gamma \\ & \pm \mu(2mgk_1 \sin\gamma \sin\beta + wk_2)mg\cos\gamma \\ & + mg\sin\gamma\sin\beta(mgk_1\sin\gamma\sin\beta + wk_2). \quad (6) \end{aligned}$$

$P_{\text{IN}}$ can be measured using a power sensor, $\gamma$ and $\beta$ can be estimated from roll, pitch, yaw measurements of an inertial measurement unit (IMU) and knowledge of the robots' reference frames. So, the friction coefficient can be estimated by calculating the roots of (6), and choosing the positive one.

### B. Temperature Effects

Power losses in a motor cause a rise of its temperature, which in turn increases the resistance of the windings and decreases the torque and speed constants [33]. The decrease in the torque constant must be compensated by an appropriate increase in the current to maintain the same torque. As a result, due to increased motor temperature, both $R_a$ and $I_a$ in (1) increase, increasing the first term that corresponds to electrical losses. Note that an increase in the current will cause an increase in the losses at the motor drivers, which will increase their temperatures even more

if they are not properly cooled. This increase in the temperature will increase the MOSFET resistances [34] inducing a further increase in the losses.

The rise in the resistance with temperature is given by

$$\mathcal{R}(T) = \mathcal{R}_0(1 + \boldsymbol{\alpha}(T - T_0)) \qquad (7)$$

where $\boldsymbol{\alpha}$ is the temperature coefficient, $T_0$ is the initial temperature at which the initial resistance $\mathcal{R}_0$ is measured. For example, $\boldsymbol{\alpha}$ for copper is known to be 0.004/°C, which means that a 100° rise in the temperature causes a 40% rise in the resistance, and also in the corresponding copper losses. The change in the motor torque and speed constants is given by a similar equation

$$k(T) = k_0(1 + \boldsymbol{\alpha}(T - T_0)). \qquad (8)$$

However, this time the temperature coefficient $\boldsymbol{\alpha}$ is negative, implying a need to increase the current and the voltage supplied to achieve the same torque and speed.

So, $k_1$ and $k_2$ in (6) can be updated as

$$k_1(T) = k_{1_0}(1 + \boldsymbol{\alpha}_R(T - T_0))(1 + \boldsymbol{\alpha}_M(T - T_0))^{-2} \quad (9)$$

$$k_2(T) = k_{2_0}(1 + \boldsymbol{\alpha}_M(T - T_0))^{-2} \qquad (10)$$

$k_{1_0}$ and $k_{2_0}$ are the motor constants of (6) measured at $T_0$, $\boldsymbol{\alpha}_R$ is the temperature coefficient for the resistance and $\boldsymbol{\alpha}_M$ is the temperature coefficient for the motor and speed constants. Using these updated values for the motor constants, it is possible to approximately calculate motor constants at different temperatures.

Note that for an exact compensation of this effect in friction estimation, as well as its effect on the total power consumption, the inner core temperature of the motors should be measured, and also the temperature of different segments of the wires, which is not practical in general and this is not possible with our current hardware. Instead, we experimentally find $\boldsymbol{\alpha}$ values that minimize the variance of the estimated friction with temperature. This approach gives sufficiently good results for moderate temperature rises. And of course the approach is valid if precise temperature measurements become available.

### C. Classification of Motion

A skid-steered robot (see Fig. 2) can be differentially driven by setting the velocities of its right- and left-side wheels ($v_1$, $v_2$), or equivalently its translational and rotational velocities ($v$, $w$). In motion, the robot rotates around the ICR, whose distance to the center of the robot is given by

$$R = \frac{v}{w}. \qquad (11)$$

The forces that should be applied by the wheels of a skid-steered robot can be analyzed in three different regions that depend on the directions and magnitudes of the side velocities $v_1$ and $v_2$.

In the first region ($R = \infty$), characterized by pure translational motion, the speeds of the left and right wheels are the same. In this setting, both wheels generate equal force, requiring equal power from their respective motors. In this configuration, the wheels are only rolling and, therefore, the motors have
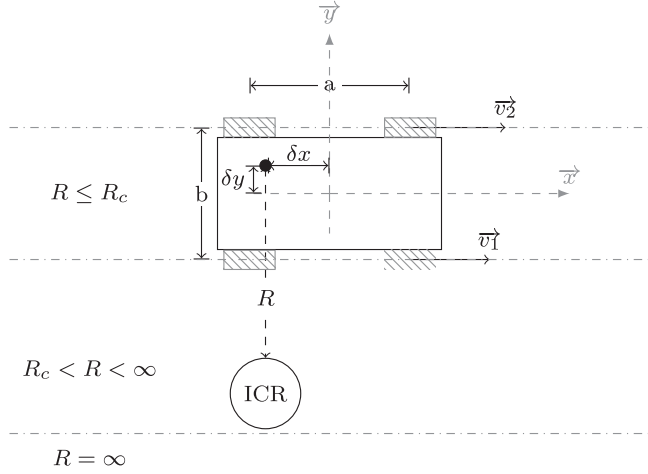
Fig. 2. Schematic of a skid-steered wheeled robot. The center of mass of the robot is indicated by the black dot at coordinates $(-\delta x, \delta y)$ with respect to the geometric center of the robot. Robot's power consumption varies considerably depending on the position of the ICR. $R_c$ corresponds to the case that the ICR is somewhere on the line connecting the right wheels.
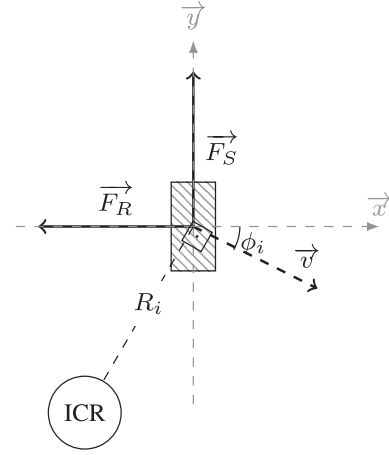


Fig. 3. Free body diagram of a wheel. The shaded rectangle shows the section of the wheel touching the ground. As the robot is forced to move along $\overrightarrow{v}$ due to a rotation around the ICR at a finite distance $R_i$, it will be subject to skid friction along its $y$-axis, and to rolling friction along its $x$-axis.

to overcome only rolling resistance. Compared to the next two regions, this is the region requiring minimum power consumption. In this region, the ICR is located at infinity.

In the second region ($R_c < R < \infty$, $R_c$ being the distance from the center of mass of the robot to the line connecting the right wheels), wheels on both sides are rotating in the same direction, but with different speeds: The ones on one side are rotating faster, resulting in skidding and motion along a curve. Therefore, the side with the faster wheels drags the other side along, applying the whole force needed to drive the robot. In this region, the slower wheels rotate due to drag from the other side. However, their speed is regulated by the motor's controller, which results in energy generation. The ICR is located between infinity and the wheels of the robot. In this mode, the robot is expected to spend considerable power, because it has to overcome skidding.

In the final region ($R \leq R_c$), the wheels on different sides rotate in opposite directions, i.e., now $v_1$ and $v_2$ have opposite signs. In this case, both wheels generate force to rotate, and the ICR is located inside the base of the robot, somewhere between its center and the wheels. If $v_1$ and $v_2$ happen to have the same magnitude, then a balanced robot rotates on the same spot and both wheels contribute with equal power. If the robot is not doing in place rotations, then the side with faster wheels is expected to be generating more power.

In the first and third regions, both motors contribute to force generation, and each motor is responsible from overcoming friction in its own wheels. However, in the second region, the active motor has to provide all the power necessary to rotate wheels of both sides, to overcome friction due to skid, and to provide the power recovered at the other motor, which acts as some kind of breaking mechanism.

### D. Modeling Skid Friction

The power balance equation for the outer side, when it is dragging the robot along, in a skid-steered mobile robot can be written as

$$P_2 - P_1 = P_S + P_R \tag{12}$$

where $P_2$ is the power that should be supplied by the active side, $P_1$ is the power generated on the inner side when the robot is operating in the second region (see Fig. 2, $R_c < R < \infty$), $P_R$ is the power that is necessary to overcome rolling friction of the wheels ($\mu_R$), which in the second region is rolling friction of both sides, i.e., all four wheels. Note that this power is generated as the controllers try to keep a fixed speed for the inner side, which is possible only by extracting power from it. $P_S$ is the power spent on skidding, i.e., by the drag of the wheels on the surface. $P_1$ has nothing to do with ground friction, so we can just subtract it from $P_2$ and do work analysis on the left out power created by the force called $F_2'$. In steady state, the force $F_2'$ is constant in magnitude, and it is opposed by an equal magnitude force, which is due to friction. Therefore, $F_2'$ can be taken equal to the equivalent friction force due to rolling friction and skid. This equivalent friction force is represented by an equivalent friction coefficient in this paper. Note that Fig. 3 idealizes the section of the wheel touching the ground with a rectangle. However, the exact shape as well as the pressure distribution depends on the surface, threads of the tire, tire pressure and tire material among others. In this paper, a lumped model is used, assuming all interactions can be modeled as a combination of friction due to rolling and skid.

For an infinitesimal rotation of $\delta\theta$, along a circle with a radius of $R$, the work done by the outer net force, and the other forces $F_S$ and $F_R$, shown in Fig. 3, corresponding to $P_S$ and $P_R$, respectively, will be

$$\sum_{i \in S_{\mathrm{OW}}} \overrightarrow{F_i'} \cdot \overrightarrow{R_i \delta\theta} = \sum_{i \in S_{\mathrm{AW}}} \overrightarrow{F_{S_i}} \cdot \overrightarrow{R_i \delta\theta} + \sum_{i \in S_{\mathrm{AW}}} \overrightarrow{F_{R_i}} \cdot \overrightarrow{R_i \delta\theta} \tag{13}$$

where $S_{\mathrm{OW}}$ and $S_{\mathrm{AW}}$ are, respectively, the set of outer and the set of all wheels, and $R_i$ is the distance between the ICR and the corresponding $i_{\mathrm{th}}$ wheel (see Fig. 3). Note that $\overrightarrow{R_i \delta\theta}$ is the

This article has been accepted for inclusion in a future issue of this journal. Content is final as presented, with the exception of pagination.

6                                                                                                    IEEE TRANSACTIONS ON ROBOTICS

distance vector perpendicular to $R_i$ and it can be approximated as a straight line for a very small $\delta\theta$. Rolling friction acts fully when the wheels move by rotating in the $x$-axis, and similarly, skid is fully in action when the wheel moves only along the $y$-axis. In a hybrid motion that forces the wheel move in none of those orthogonal directions, the wheel will be subject to both rolling and skidding, however, each will partially contribute to the overall motion. The contribution of each will be proportional to their components that are parallel to the direction of motion ($\overrightarrow{v}$). The same is valid for $\overrightarrow{F'_i}$, which can transfer energy only through the rotation of the wheels.

Thinking in terms of infinitesimal time steps, initially $F_S$ does not exist. $F_2$ is generated, which causes rotations of the outer wheels, which in turn causes a motion of the robot's body, moving the inner wheels and activating $F_B$, the breaking force. The balance of these forces causes the robot to move along a curve, creating skid.

Friction force is normally defined as $F = \mu N$, where $N$ is the normal force. In an unbalanced mobile robot, the normal force acting on each wheel is expected to be different and directly correlated with the location of the center of mass of the robot. Assuming that the center of mass is displaced by $\delta x$ along the $x$-axis and by $\delta y$ along the $y$-axis (see Fig. 2), the normal force on wheel $i$ will be

$$N_i = \left(\frac{1}{2} \pm \frac{\delta x}{a}\right)\left(\frac{1}{2} \pm \frac{\delta y}{b}\right)N \qquad (14)$$

with $N$ given by the equation $N = mg\cos\gamma$, where $m$, $g$, and $\gamma$ are mass of the robot, the gravitational constant, and the angle of the inclined plane below the robot, respectively. And $a$ and $b$ are the horizontal and the vertical distances between the wheels, as shown in Fig. 2. The $\pm$ operations in (14) are chosen according to the distance of the wheel to the center of mass, both operations are $+$ for the closest wheels, and they are $-$ for the farthest wheels.

Using (13) and (14), after some algebraic simplifications, the following equation is obtained for the friction coefficient of a skid-steered wheeled robot

$$\mu = \frac{R_0 + \delta y}{R_0 + \frac{b}{2}}\mu_R + \frac{2a\left(\frac{1}{4} - \left(\frac{\delta x}{a}\right)^2\right)}{R_0 + \frac{b}{2}}\mu_S \qquad (15)$$

where $R_0$ is the distance between the geometric center of the robot and the ICR. The coefficients $\mu_R$ and $\mu_S$ correspond to friction due to roll and skid forces, respectively.

Derivation of (15) accounts for extra slippage due to the fact that wheels of each side have to rotate at the same speed, and stores this in $\mu_R$, which is not portable to different center of mass locations in its current form. To make $\mu_R$ portable, it was experimentally found out that $\mu_R$ should be corrected by the ratio of the distance between the wheels and the location of the center of mass to the distance between the wheels and the geometric center. This gave us the following improved equation

$$\mu = \frac{R_0 + \delta y}{R_0 + \frac{b}{2}}\sqrt{\frac{\left(\frac{a}{2} - |\delta x|\right)^2 + \left(\frac{b}{2}\right)^2}{\left(\frac{a}{2}\right)^2 + \left(\frac{b}{2}\right)^2}}\mu_R + \frac{2a\left(\frac{1}{4} - \left(\frac{\delta x}{a}\right)^2\right)}{R_0 + \frac{b}{2}}\mu_S. \qquad (16)$$



(a)



(b)

Fig. 4. (a) Husky, the skid-steered wheeled robot used in the experiments. (b) Power measurement board designed and used for the robot.

From (16), it can be easily seen that as the radius of curvature $R_0$ increases, the coefficient of $\mu_S$ decreases, and the coefficient of $\mu_R$ increases, implying that the wheels skid less and roll more, which is the expected behavior. As $R_0$ decreases, the inverse happens: the robot skids more. This can be seen by the increase of the coefficient of $\mu_S$ and decrease of the coefficient of $\mu_R$ in (16). This equation also gives clues about how friction of a skid-steered robot changes as its center of mass location changes. For example, if $\delta x = |\frac{a}{2}|$, i.e., the center of mass is exactly on the front or back axis, skid simply vanishes, implying that the robot behaves like a differentially driven robot. Another conclusion from (16) is on the effect of geometry on skid behavior. A longer skid-steered robot, having a larger $a$, will be subject to larger skid forces. On the other hand, a wider robot will be subject to less skid, due to larger $b$.

Power consumed by a skid-steered wheeled robot in the second operating region can easily be found using (6) together with the friction value estimated from (16). Power consumed in the first operating region requires taking into account the power consumed by the inner side as well. For this, the friction experienced by the inner side has to be found and used in (6), and then, the estimated power should be added to the power found for the outer side. As to be seen in Section V, in the first operating region, a constant friction value for the inner side gives satisfactory results.

## IV. EXPERIMENTAL SETUP

In this paper, for the purpose of power consumption characterization of a skid-steered wheeled robot, a Clearpath Husky A200 was used [see Fig. 4(a)]. The distance between the centers of the left and right wheels $b$ as well as the distance between the centers of wheels of one side $a$ are approximately
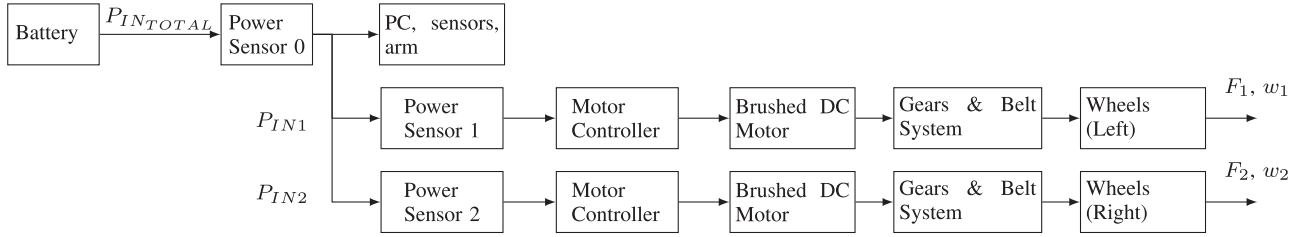
Fig. 5.    Power measurement system.

0.54 m. The original robot was customized by extending it with a sensor bridge, and an arm increasing its weight from 50 kg to approximately 90 kg. Husky has two 24-V brushed dc motors with a rated current of 7.9 A driving wheels of each side. The outer case of each motor is instrumented with a thermistor providing an estimate of the motor's temperature. The motors are equipped with gearboxes having 79 : 1 gear ratio letting them provide torque up to 50 N·m. On each side, a motor is directly coupled to one of the wheels through a shaft, and the other wheel is connected to this shaft by a belt. Each motor is controlled by a Stellaris MDL-BDC24 brushed dc motor controller from Texas Instruments. The motor controllers can provide up to 40-A continuous current. They have built-in fans to help cooling and they have also built-in fault protection mechanism for over temperature as well as over current. The robot already has a built-in power consumption measurement system. However, during the initial experiments, it was noticed that this was not accurate and, therefore, a new set of custom power measurement boards [see Fig. 4(b)] was designed and integrated. These boards are based on INA226 bidirectional current and power sensor from Texas Instruments. The sensor can measure up to 36 V, and has a resolution of 16 bits with configurable range to measure current. The boards were connected through an $I^2C$ bus to an Arduino board. The Arduino board was polled by a robot operating system (ROS) process running on a Brix i7 computer that controls the robot. After polling, the data were published as a ROS topic. A schematic of the location of the custom power measurement system can be seen in Fig. 5. In this paper, we measured $P_{\rm IN}$ at the input of each motor driver, as well as the corresponding wheel encoder value, leaving the motor currents and torque to the black-box model. In addition to the power and encoder data, attitude data were collected using a state-of-the-art IMU from X-Sense, namely MTi-300. The IMU provided heading, yaw, and pitch measurements, which were required to calculate the forces on the robot on the terrain, as well as accelerations in different axes. The IMU communicates with the main computer through USB at 50 Hz, though it is capable of communicating a full stream of data at up to 400 Hz.

Experiments were run both indoors and outdoors. The indoor environments were flat surfaces tiled with marble or wood. The outdoor environment was a terrain with a slope varying up to 17°.

In order to see the effect of the location of the center of mass on the friction model, different weights with 14 or 28-kg mass were put on the robot in different positions. Due to its batteries, the robot's center of mass is already a little on the back (by
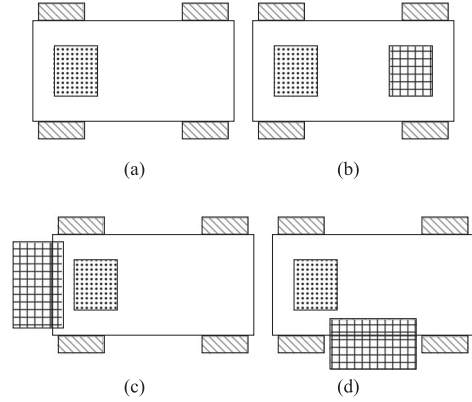


Fig. 6.    Robot with three different weight combinations. The dotted rectangle shows the batteries, weighing 12 kg, and the grids show position of the extra weights used. (a) No extra weight (Configuration A), (b) 14 kg on the front (Configuration B), (c) 28 kg on the back (Configuration C), and (d) 28 kg on the side (Configuration D).

3 cm) without any add-ons [Configuration A, shown in Fig. 6(a)]. Weights were put on the robot in three different positions: on the front [Configuration B, Fig. 6(b)] to move the center of mass to the center; on the back [Configuration C, Fig. 6(c)], to shift the center of mass more to the back (by 11 cm), and on the outer side [Configuration D, Fig. 6(d)] to shift the center of mass to the edge of the robot (by 8 cm).

During the tests, the robot was driven in straight lines, rotated in place and also driven along paths of varying radius of curvature, corresponding to different ICRs. For this, the commanded values of the rotational and translational speeds of the robot were increased uniformly. However, the speeds of the wheels of each side were limited by the firmware to 1 m/s. Although we were able to command the robot speeds that require one of the wheels to move at linear speeds higher than 1 m/s, the firmware just ignored the commanded values and drove the corresponding wheel at a speed close to the maximum, which in turn resulted in some irregularities in the measured speeds. Each increment of the speeds is defined as an experiment in this paper, and the experiments lasted one full rotation around the ICR. Then, the transients corresponding to the beginning and end of the experiment, where the robot is, respectively, speeding up and down, were filtered out.

## V. RESULTS AND DISCUSSION

Direct measurement of friction coefficients is not feasible in dynamic environments such as the operating region of a robot,
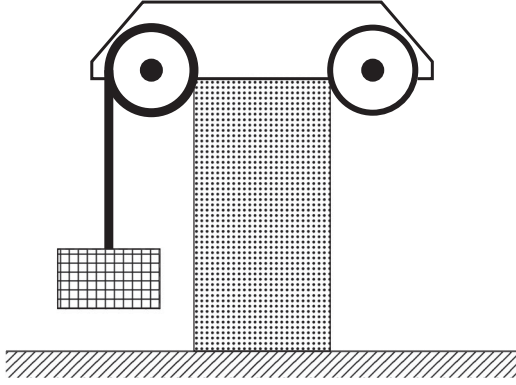
Fig. 7. Schematic of the setup used to measure the equivalent motor parameters $k_1$ and $k_2$. The robot was put high above the ground, a weight was tied to one of the wheels and the robot was commanded to move the weight up at various constant speeds.

TABLE I
MOTOR CONSTANTS AS MEASURED THROUGH DIFFERENT WHEELS

|  | Front | Back | Mean |
|---|---|---|---|
| M1 (Left motor) | | | |
| $k_1$: | 0.0023 | 0.0023 | 0.0023 |
| $k_2$: | 1.7144 | 1.7172 | 1.7158 |
| | | | |
| M2 (Right motor) | | | |
| $k_1$: | 0.0019 | 0.0013 | 0.0016 |
| $k_2$: | 1.7118 | 1.8327 | 1.7723 |



Fig. 8. Power measured and the corresponding fit when the robot was asked to pull up a known weight at different speeds with its front left wheel, allowing us to estimate $k_1$ and $k_2$ of (2). Curves for measurements through other wheels are quite similar to this one.

requiring an alternative way to measure it. Therefore, in this paper, to estimate friction $\mu$, we make use of (6). The coefficients of (16), $\mu_r$ and $\mu_s$, were estimated by the minimization of least squares error on the collected friction data. Motor parameters $k_1$ and $k_2$ are estimated using the experimental setup described in Section V-A. In order to compensate for temperature variations, $k_1$ and $k_2$ were updated according to (9) and (10). This as well as the effect of temperature to the total power consumption of a robot are presented in Section V-B. Then, in Section V-C, estimated friction values and their statistical summaries are given and the estimated values are compared to the values predicted using (16). This section also includes the estimated power consumption values, which are calculated using a hybrid approach. The power consumption is estimated using the predicted friction values for $R \geq Rc$. For $R < Rc$, the power consumption was estimated using both the estimated friction values, which are valid just for the outer side in this case, and the mean value of friction measured for $R < Rc$ for the inner side.

### A. Estimation of Equivalent Motor Parameters

Proper measurement of $k_1$ and $k_2$ of (2) is necessary for a more realistic and comparable estimation of the friction coefficients. One way to measure the coefficients is to measure the motor torque and speed constants, the motor resistance, and then the efficiencies of the gearboxes and the belts connecting the wheels. This approach is time consuming and invasive, requiring isolating each part of the drive mechanism from the rest. Instead of this, an indirect approach was followed in this paper, where the drive system starting from power input up to the wheels is considered as a single piece, and the equivalent coefficients are measured. This was achieved with the setup shown in Fig. 7. The robot was put 1.5 m above the ground, and then a known weight, a 6.9-kg battery was tied to one of the wheels with a long rope. Afterward, the robot was commanded to rotate the wheels at constant speed, in effect lifting the weight. This was done for seven different constant speeds, giving us seven independent measurements for (2). Then, those measurements were combined using least squares to obtain $k_1$ and $k_2$ at temperature $T_0$, which are $k_{1_0}$ and $k_{2_0}$ in (9) and
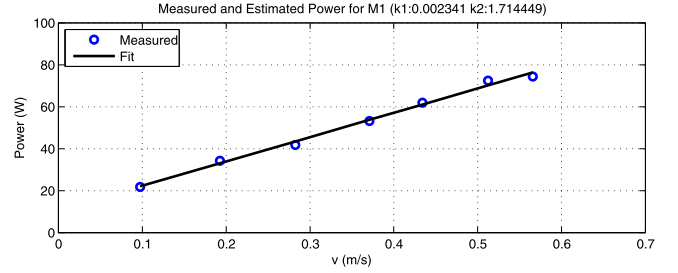
(10). This procedure was repeated for all four wheels, providing the data given in Table I. In an ideal system, it would be expected to have the same $k_1$ and $k_2$ for both motors, irrespective of the wheels used in the measurement. However, there are some differences between the left and right motors, and specifically between measuring through the front and through the back wheels for the right side. $k_1$ changes from 0.0019 to 0.0013 for the right side, whereas it was constant at 0.0023 for the left side. Similarly, $k_2$ changes from 1.7118 to 1.8327 for the right side, whereas the change is much smaller for the left side, from 1.7144 to 1.7172. This is mainly due to the brand and age of the belt used on the right side, which is quite old compared to the belt on the other side. In order to not complicate the model, the mean values were used for each side. As can be seen in Fig. 8, the power consumption is linear in wheel velocity for a given load, as is predicted by (2).

### B. Temperature Effects

In order to see the effect of the temperature on the losses, and on the estimated effective friction coefficient, the robot was driven around its own axis for 23 min at 1 rad/s. During this test, the temperatures of the drivers rose from 24 to 36 °C [see Fig. 9(a)], the rise being mainly restricted by the fans of the motor drivers. The motor temperatures were measured using the thermistors connected to their cases. The rise in the temperature of the motors, which have no special cooling mechanism, was much higher, rising from 20 to 76 °C [see Fig. 9(a)]. The power consumed by the drive system, which includes the losses and the ground friction, increased from 106 to 150 W for one side, and from 116 to 193 W for the other side [see Fig. 9(b)]. As a

This article has been accepted for inclusion in a future issue of this journal. Content is final as presented, with the exception of pagination.

DOGRU AND MARQUES: PHYSICS-BASED POWER MODEL FOR SKID-STEERED WHEELED MOBILE ROBOTS 9
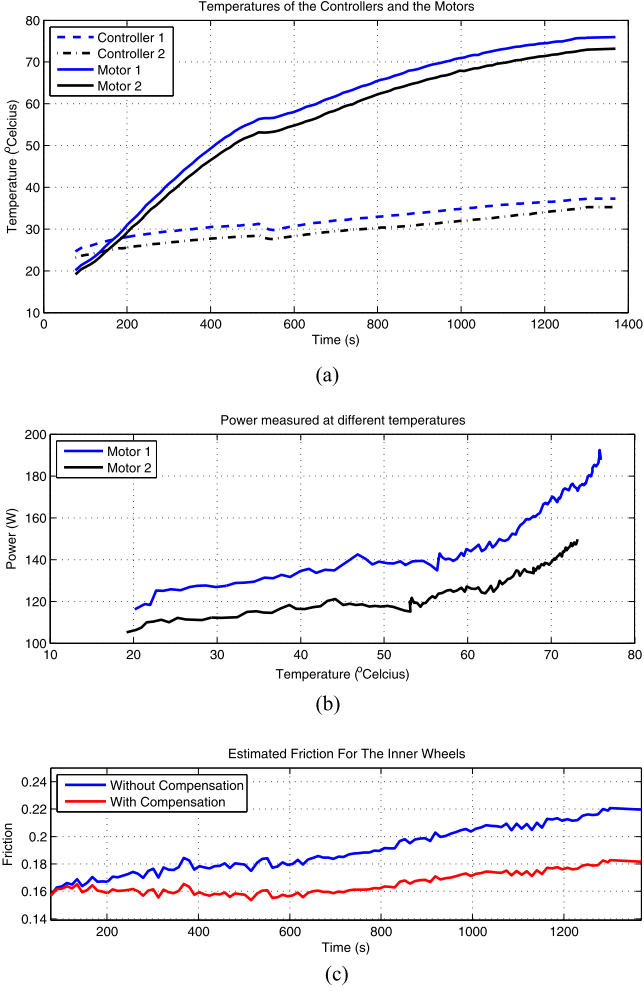


Fig. 9. Robot rotated continuously around its center for 23 min giving (a) temperatures of the motor controllers and the motors as a function of times, the irregularity around 550 s is due to stopping and rebooting the robot for a battery change, (b) powers as a function of temperature, and (c) estimated friction coefficient for M1 without and with temperature compensation.
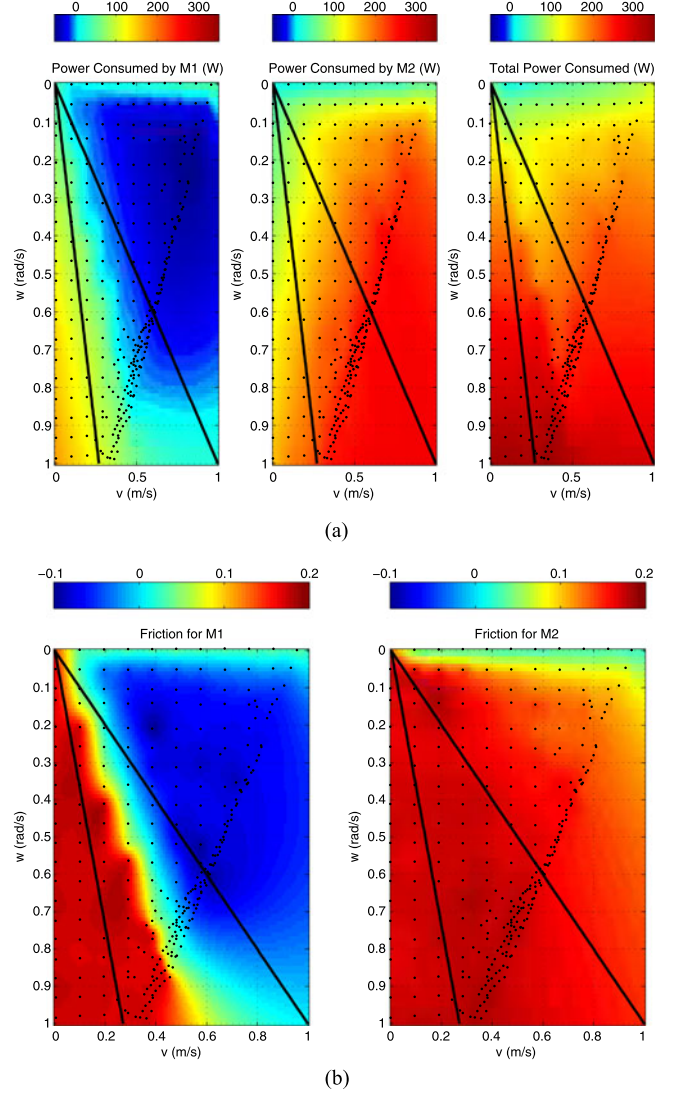


Fig. 10. (a) Power consumed by each motor on marble tiled horizontal floor (Configuration B), (b) and the corresponding friction values estimated using the method described in Section III-A. The lines on each subfigure correspond to $R = R_c$ and $R = 1$, respectively. The slower wheels (shown as M1) start generating power a little after $R > R_c$, as can be seen by the blue region in the top left figure.

result, the effective friction changed from 0.16 to 0.22, which means that temperature compensation is a must.

It can be seen that power is not linear with temperature globally, but the temperature range can be divided into two linear segments at around 60 °C. As a result in Fig. 9(c), it can be seen that temperature compensation works properly for temperatures below 65 °C, the range for which the corresponding $\alpha$ values were selected. Despite the fact that the temperature sensor used was placed on the case of the motors, the described temperature compensation improved the model. It is clear that a more accurate measurement of the motor temperatures will improve the fitness of the model even further.

### C. Friction Estimation and Prediction

In Fig. 10, the power consumption of the robot for different rotational and translational velocity pairs as well as the friction estimated through (6) are given. It can be seen that the power consumption of the first motor is negative for large radius of curvatures [see Fig. 10(a)], starting at $R$, measured as ratio of the

translational speed obtained through the calibrated encoders and the rotational speed obtained through the IMU, a little larger than $R_c$, indicating that power is flowing from the motor back to the batteries. This is of course reflected in corresponding estimated friction values too [see Fig. 10(b)]. Note that on Husky, the motor drivers are connected to the same power bus. Hence, power generated by the inner side is automatically consumed by the outer side, reducing the total power drawn from the battery.

The minimum (Min), maximum (Max), mean, standard deviation (Std), and range, which is defined as $\text{Max} - \text{Min}$, of the estimated friction coefficients given in Fig. 10(b) are summarized in Table II for different ranges of $R$ for both the faster (M2) and the slower (M1) sides. $R = 0$ corresponds to the case when the ICR is at center of mass of the robot, $R \leq R_c$

TABLE II
FRICTION COEFFICIENT OF BOTH SIDES CORRESPONDING TO DIFFERENT
ICR LOCATIONS (CONFIGURATION B)

| | $R = 0$ | $R \leq R_c$ | $R_c < R < \infty$ | $R = \infty$ |
|---|---|---|---|---|
| **M1:** | | | | |
| Min: | 0.1670 | 0.1670 | $-0.0973$ | 0.0355 |
| Max: | 0.1779 | 0.1779 | 0.1840 | 0.0417 |
| Mean: | 0.1734 | 0.1742 | $-0.0252$ | 0.0381 |
| Std: | 0.0044 | 0.0034 | 0.0687 | 0.0018 |
| Range: | 0.0109 | 0.0109 | 0.2813 | 0.0062 |
| **M2:** | | | | |
| Min: | 0.1644 | 0.1644 | 0.0232 | 0.0232 |
| Max: | 0.1738 | 0.1738 | 0.1787 | 0.0275 |
| Mean: | 0.1703 | 0.1706 | 0.1340 | 0.0248 |
| Std: | 0.0034 | 0.0027 | 0.0492 | 0.0014 |
| Range: | 0.0094 | 0.0094 | 0.1555 | 0.0043 |

corresponds to the case when the ICR is under the base of the robot. In both cases, both wheels are consuming power. $R_c < R < \infty$ corresponds to the case when the ICR is outside the robot base, in which case the wheels of the slower side are breaking the platform and generating power, as can be also seen by the mean/min negative friction coefficients of the slower wheel. $R = \infty$ corresponds to the case of straight line motion, in which case both wheels are consuming power.

Examination of Table II reveals that friction varies very little for straight line motion ($R = \infty$), just by 0.0062 for the first side, and by 0.0043 for the second. And although not that small, the variance is small for the outer side (M2) when the ICR is inside the robot base ($R < R_c = 0.27$), the difference between the smallest and largest values is 0.0094 where the mean is 0.1703, whereas the variance for the slower side is 0.0109. The range of the friction coefficient is much larger when ICR is outside the robot base, it varies from 0.0232 to 0.1787 for the faster side, and between positive and negative values for the slower side. These observations indicate that, although constant values can be utilized for friction at a fixed radius of curvature, such as 0, or $\infty$, using a constant is not an acceptable approach for other ranges of $R$, specifically if it corresponds to an ICR outside the robot base.

Comparing the power consumption for different center of mass locations (see Fig. 11) it can be seen that the robot consumes least power when the center of mass is shifted back [see Fig. 11(b)], despite its higher weight compared to the balanced case [see Fig. 11(a)]. The robot consumes considerably more power when the center of mass is on the side [see Fig. 11(c)], which can be seen by comparing, for example, the region between experiments 0 and 10 corresponding to $v = 0.0$ m/s. The robot consumes more than 300 W when the center of mass is on the side, and up to 250 W when the center of mass is at the center but the robot is 14 kg lighter. It consumes less, only up to 200 W, when the center of mass is at the back and the robot is with 28 kg of extra weight, and even when rotating faster.

The variances in the power consumption for different center of mass locations are also seen in frictions estimated using (6) (see Fig. 11). The robot has least friction when the center of
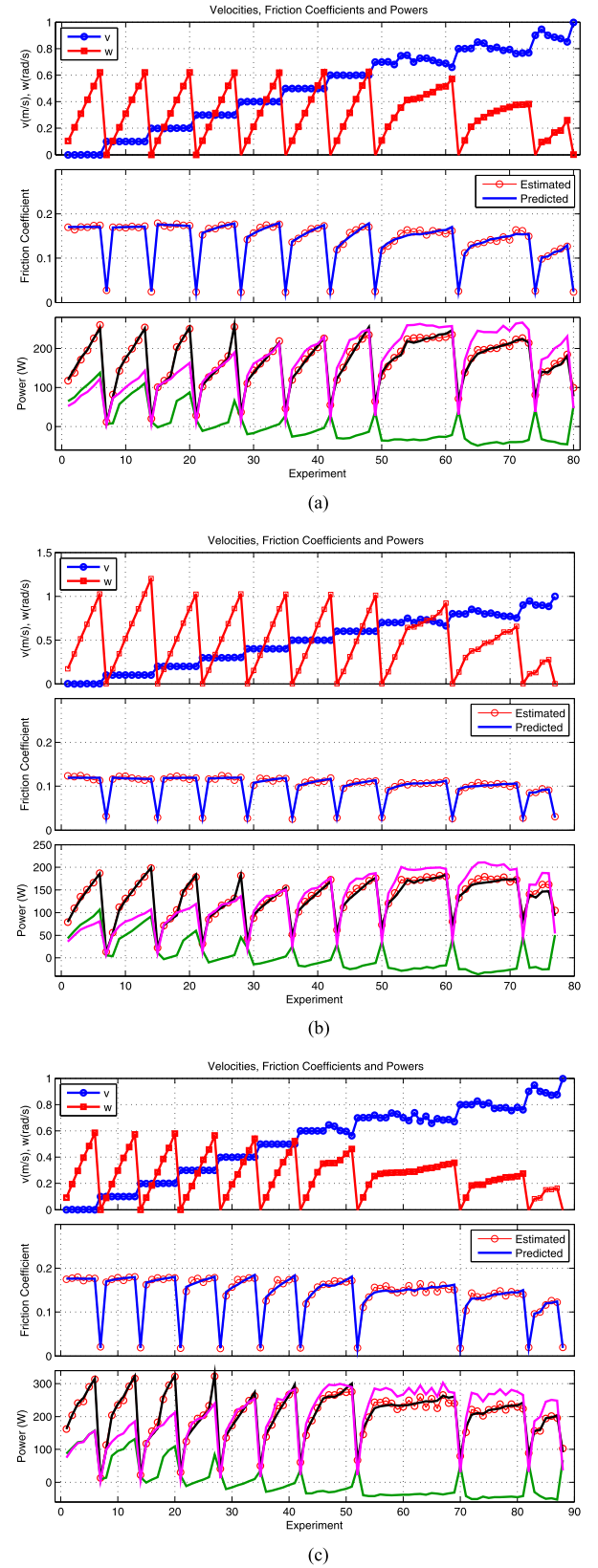


Fig. 11. Velocities, friction coefficients, and power consumption on marble surface with different center of mass configurations. The measured total power values are shown with a red circle, and the total powers predicted by this paper are shown with the black curve. The magenta and the green curves show the power consumption of the outer and inner sides. (a) Configuration B. (b) Configuration C. (d) Configuration D.

This article has been accepted for inclusion in a future issue of this journal. Content is final as presented, with the exception of pagination.

DOGRU AND MARQUES: PHYSICS-BASED POWER MODEL FOR SKID-STEERED WHEELED MOBILE ROBOTS 11

TABLE III
NORMALIZED ERRORS (%) IN FRICTION COEFFICIENT ESTIMATION OF
DIFFERENT TRANSLATIONAL VELOCITIES

| v (m/s) | 0.00 | 0.10 | 0.20 | 0.30 | 0.40 | 0.50 | 0.60 | 0.70 | 0.80 | 0.90 |
|---|---|---|---|---|---|---|---|---|---|---|
| Marble (B) | 1.28 | 0.64 | 1.34 | 1.54 | 2.68 | 1.36 | 3.55 | 4.32 | 2.66 | 2.27 |
| Marble (C) | 3.07 | 2.17 | 1.71 | 2.50 | 3.27 | 3.10 | 2.34 | 1.54 | 3.25 | 1.29 |
| Marble (D) | 1.14 | 1.26 | 1.67 | 3.74 | 3.26 | 3.49 | 3.09 | 4.38 | 3.93 | 1.95 |
| Soil | 6.41 | 2.83 | 6.19 | 6.56 | 14.06 | 5.60 | 8.69 | 5.72 | 5.96 | — |

TABLE IV
NORMALIZED ERRORS (%)

| Surface | Friction | Power |
|---|---|---|
| Marble (B) | 2.38 | 3.29 |
| Marble (C) | 2.45 | 3.61 |
| Marble (D) | 3.11 | 4.00 |
| Soil | 7.81 | 11.85 |
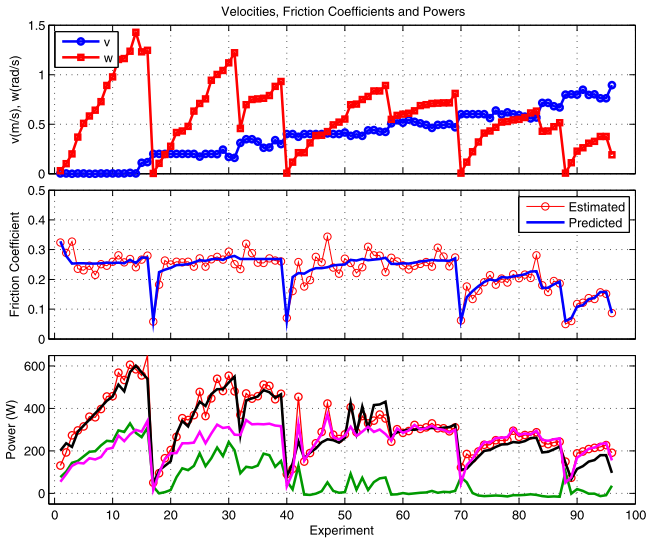


Fig. 12. Velocities, friction coefficients, and power consumption on soil.



Fig. 13. Coefficients of the friction fit function for different configurations.



Fig. 14. Comparison of the proposed model with the friction model based on shear displacement for $v = 0.5$ m/s. (a) Velocities. (b) Power consumption.
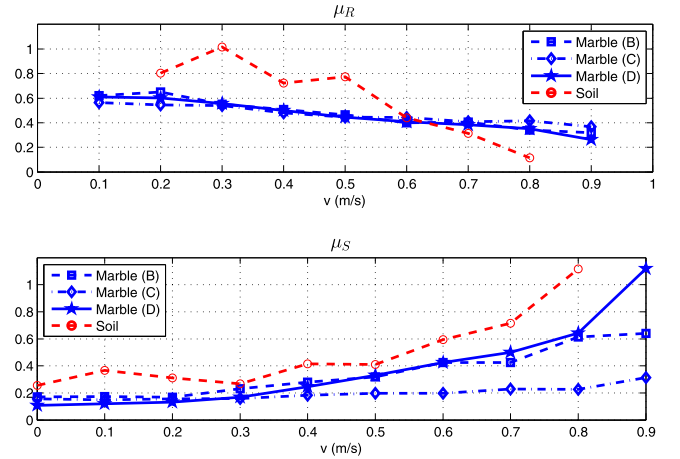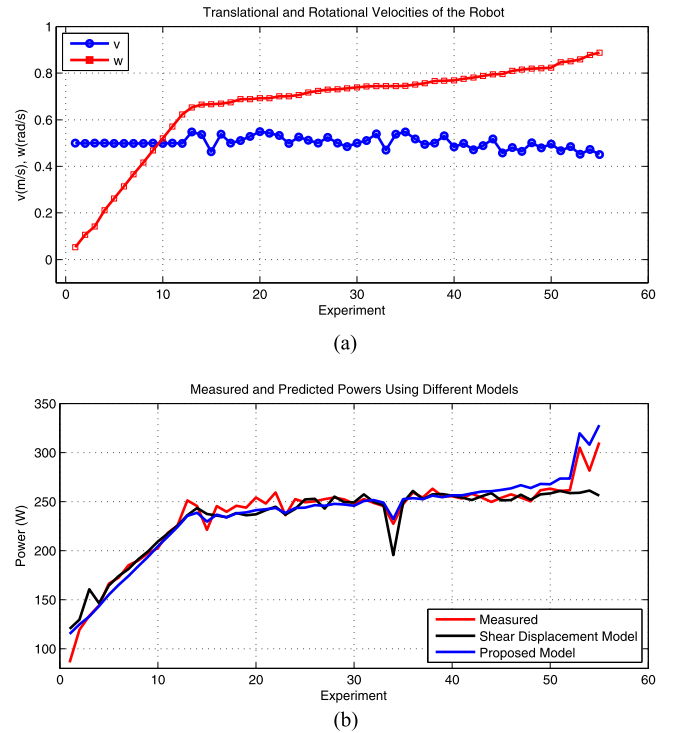
mass is on the back, in configuration C [see Fig. 11(b)]. As can be seen in these plots, and also in the error values given in Tables III and IV, the proposed model, which predicts friction using (16) with $\mu_R$ and $\mu_S$ estimated for the corresponding speed range, accurately matches the data. It is able to estimate both the friction and the total power consumption. Note that the errors are calculated as

$$e = \frac{|\mu_{\text{predicted}} - \mu_{\text{estimated}}|}{\mu_{\text{estimated}}} \times 100. \qquad (17)$$

The changes in friction as a function of the center of mass location are already predicted by (16), according to which the total friction is expected to decrease as the center of mass is moved forward or backward. Similarly, (16) predicts that total friction should increase if the center of mass is moved to the side, closer to the wheels of the robot.

Errors in the estimated friction for soil (see Fig. 12) are considerably higher, which is due to the soft soil and varying amount of grass on the test field, which can be sufficiently handled by smoothing the measurement data.

Dependence of friction on speed is apparent in Figs. 11 and 12, as well as the coefficients of (16) given in Fig. 13. As was previously mentioned, rubber friction depends on sliding speed and, therefore, this behavior is already expected.

Examination of Fig. 13 reveals that the coefficients $\mu_R$ and $\mu_S$ of (16) are close to each other for different weight configurations on the same surface, implying that if the change in the center of mass location is known, friction measurements from a different configuration can easily be used in energy efficient planning. $\mu_S$ for larger speeds does not match well, implying that the model given in (16) can still be improved. $\mu_S$ and $\mu_R$ for soil do

not match the others, which is expected because it is a different surface. However, the coefficients have the same tendencies, $\mu_R$ decreases, and $\mu_S$ increases with speed.

In order to compare the performance of the proposed model with the model based on shear displacement [22], the power consumption for different radius of curvatures at $v = 0.5$ m/s and symmetric weight distribution (Configuration B) was predicted using both models, and the results are presented in Fig. 14. The mean absolute values of the errors were found to be 7 W for the proposed model and 8 W for the model based on shear displacement, showing that both models are able to estimate the power consumption accurately.

## VI. Conclusion

This paper has studied and characterized the power consumption of a skid-steered wheeled mobile robot through friction coefficients. For this purpose, dense datasets were collected by varying the radius of curvature, the velocities, the surface, the mass, the center of mass location, and the operating temperature. The datasets showed that friction varies with radius of curvature and with speed of the robot. The data also showed that the friction, and as a result the power consumed by a skid-steered robot varies a lot with the location of the center of mass.

All these observations led to the development of a physical model showing how friction coefficient changes with radius of curvature and center of mass location. The physical model showed that the friction coefficient can be expressed as the sum of two coefficients, one expressing roll and the other expressing skid. Dependency of friction coefficient on speed was not integrated into the physical model, but it was shown that the developed model can be applied successfully for different velocity ranges, requiring usage of different coefficients for different velocities. The proposed physical model allows accurate estimation of how friction, and as a result power consumption, changes when the radius of curvature changes.

The proposed model describes how friction changes as the center of mass location changes, allowing friction coefficients obtained at one center of mass configuration to be used with a different one. Center of mass location changes are expected for a load carrying platform, such as a skid steer loader. The change is also expected when a robot is equipped with new hardware, such as a heavy arm, or extra batteries for longer missions, among many other reasons. The model shows that as the center of mass of the robot moves closer to the back or front wheels, skid friction decreases, eventually vanishing when the center of mass is on the axis connecting the wheels on the back, or the ones on the front. Vanishing of skid makes a skid-steered platform equivalent to a differentially driven platform in terms of power consumption, and even traction. Another prediction of the model is that friction increases as the center of mass moves closer to the left or right edges of the robot. All those predictions of the proposed model have been experimentally verified in this paper.

The proposed model also makes predictions about the dependence of friction on platform geometry, namely, the distance between the front and back wheels, as well as the distance between the wheels of one side. These distances determine the slip angles of the wheels for a given ICR location. Since slip angles are the main cause of skid in these platforms, friction of different sized platforms for the same ICR will be different. The model predicts that longer platforms will experience more skid, whereas wider ones will be experiencing less.

The paper measures the friction coefficient indirectly through the powers fed to the motor drivers, wheel encoder values, as well as roll, pitch, and yaw measurements of the robot. Thanks to the attitude measurements of the robot, friction measurement is able to take into account terrain relief, allowing real-time or predicted power consumption estimation irrespective of the heading of the robot on the field. Although this black-box approach to measure friction is prone to error when the temperatures of the motors change under load, the paper has shown how this problem can be mitigated even in real time.

The paper has also shown an easy way to measure the equivalent motor parameters that include motor parameters as well as efficiencies of the drive system using only the powers fed to the motor drivers and encoder values. This way, the methods described in this paper can easily be applied to other off-the-shelf skid-steered platforms.

This paper has shown that the temperatures of the motors as well as the motor drivers are important contributors to the losses and as a result to the total power consumption of the robot. These temperatures tend to rise over time during a mission, and this rise increases the losses even further and as a result the power consumption increases even more. To avoid extra power losses due to heated components in the power train, proper cooling should be utilized, especially in robots operating under heavy load or in long missions.

This paper could be extended in various ways, both by improving and using the proposed model. The proposed model could be tested at higher speeds, and the transients could be taken into account. Contribution of the transients to the total power consumption may become significant when the robot has to perform maneuvers requiring many speed changes. Transients may also cause very high, although short, starting currents. These high currents may overload the driver and the battery of the platform. Hence, finding maneuvers that will limit them is important.

## References

[1] F. B. Hoogterp and W. R. Meldrum, "Differential torque steering for future combat vehicles," SAE, Troy, MI, USA, SAE Technical Paper, Tech. Rep. 1999-01-3740, 1999.

[2] W. R. Meldrum, F. B. Hoogterp, and A. R. Kovnat, "Modeling and simulation of a differential torque steered wheeled vehicle," Defense Technical Information Center, Warren, MI, USA, DTIC Document, Tech. Rep. ADA408819, 1999.

[3] B. Maclaurin, "Comparing the steering performances of skid and Ackermann-steered vehicles," *Proc. Inst. Mech. Eng., Part D, J. Autom. Eng.*, vol. 222, no. 5, pp. 739–756, 2008.

[4] V. Berenz, F. Tanaka, and K. Suzuki, "Autonomous battery management for mobile robots based on risk and gain assessment," *Artif. Intell. Rev.*, vol. 37, no. 3, pp. 217–237, 2012.

[5] A. Sadrpour, J. Jin, and A. Ulsoy, "Mission energy prediction for unmanned ground vehicles," in *Proc. 2012 IEEE Int. Conf. Robot. Autom.*, May 2012, pp. 2229–2234.

[6] A. Sadrpour, J. Jin, and A. Ulsoy, "Experimental validation of mission energy prediction model for unmanned ground vehicles," in *Proc. 2013 Amer. Control Conf.*, Jun. 2013, pp. 5960–5965.

[7] R. Parasuraman, K. Kershaw, P. Pagala, and M. Ferre, "Model based on-line energy prediction system for semi-autonomous mobile robots," in *Proc. 2014 5th Int. Conf. Intell. Syst. Model. Simul.*, Jan. 2014, pp. 411–416.

[8] J. Broderick, J. Hartner, D. Tilbury, and E. Atkins, "Modeling and simulation of an unmanned ground vehicle power system," *Proc. SPIE*, vol. 9084, 2014, Art. no. 908406.

[9] Y. Mei, Y.-H. Lu, Y. Hu, and C. Lee, "A case study of mobile robot's energy consumption and conservation techniques," in *Proc. 12th Int. Conf. Adv. Robot.*, Jul. 2005, pp. 492–497.

[10] J. Brateman, C. Xian, and Y.-H. Lu, "Energy-efficient scheduling for autonomous mobile robots," in *Proc. 2006 IFIP Int. Conf. Very Large Scale Integr.*, Oct. 2006, pp. 361–366.

[11] Y. Mei, Y.-H. Lu, C. Lee, and Y. Hu, "Energy-efficient mobile robot exploration," in *Proc. 2006 IEEE Int. Conf. Robot. Autom.*, May 2006, pp. 505–511.

[12] C. Ooi and C. Schindelhauer, "Minimal energy path planning for wireless robots," *Mobile Netw. Appl.*, vol. 14, no. 3, pp. 309–321, 2009.

[13] Z. Sun and J. Reif, "On finding energy-minimizing paths on terrains," *IEEE Trans. Robot.*, vol. 21, no. 1, pp. 102–114, Feb. 2005.

[14] J. Broderick, D. Tilbury, and E. Atkins, "Optimal coverage trajectories for a UGV with tradeoffs for energy and time," *Auton. Robots*, vol. 36, no. 3, pp. 257–271, 2014.

[15] A. Sharma, N. Gupta, and E. G. Collins, Jr., "Energy efficient path planning for skid-steered autonomous ground vehicles," in, vol. 8045, 2011, Art. no. 80450P.

[16] N. Gupta, C. Ordonez, and E. G. Collins, "Dynamically feasible, energy efficient motion planning for skid-steered vehicles," *Auton. Robots*, vol. 41, no. 2, pp. 453–471, 2017.

[17] S. Dogru and L. Marques, "Energy efficient coverage path planning for autonomous mobile robots on 3D terrain," in *Proc. 2015 IEEE Int. Conf. Auton. Robot Syst. Competitions*, Apr. 2015, pp. 118–123.

[18] T. Guo and H. Peng, "A simplified skid-steering model for torque and power analysis of tracked small unmanned ground vehicles," in *Proc. Amer. Control Conf.*, Jun. 2013, pp. 1106–1111.

[19] J. A. Broderick, D. M. Tilbury, and E. M. Atkins, "Characterizing energy usage of a commercially available ground robot: Method and results," *J. Field Robot.*, vol. 31, no. 3, pp. 441–454, 2014.

[20] J. Morales, J. Martinez, A. Mandow, A. Garcia-Cerezo, and S. Pedraza, "Power consumption modeling of skid-steer tracked mobile robots on rigid terrain," *IEEE Trans. Robot.*, vol. 25, no. 5, pp. 1098–1108, Oct. 2009.

[21] J. Pentzer, S. Brennan, and K. Reichard, "On-line estimation of vehicle motion and power model parameters for skid-steer robot energy use prediction," in *Proc. Amer. Control Conf.*, Jun. 2014, pp. 2786–2791.

[22] W. Yu, O. Y. Chuy, Jr., E. G. Collins, Jr., and P. Hollis, "Analysis and experimental verification for dynamic modeling of a skid-steered wheeled vehicle," *IEEE Trans. Robot.*, vol. 26, no. 2, pp. 340–353, Apr. 2010.

[23] O. Y. Chuy, Jr., E. G. Collins, W. Yu, and C. Ordonez, "Power modeling of a skid steered wheeled robotic ground vehicle," in *Proc. IEEE Int. Conf. Robot. Autom.*, May 2009, pp. 4118–4123.

[24] K. A. Grosch, "The relation between the friction and visco-elastic properties of rubber," *Proc. Roy. Soc. London. Ser. A, Math. Phys. Sci.*, vol. 274, no. 1356, pp. 21–39, 1963.

[25] B. Lorenz, Y. R. Oh, S. K. Nam, S. H. Jeon, and B. N. J. Persson, "Rubber friction on road surfaces: Experiment and theory for low sliding speeds," *J. Chem. Phys.*, vol. 142, no. 19, 2015, Art. no. 194701.

[26] I. Duleba and J. Sasiadek, "Nonholonomic motion planning based on Newton algorithm with energy optimization," *IEEE Trans. Control Syst. Technol.*, vol. 11, no. 3, pp. 355–363, May 2003.

[27] C. H. Kim and B. K. Kim, "Energy-saving 3-step velocity control algorithm for battery-powered wheeled mobile robots," in *Proc. 2005 IEEE Int. Conf. Robot. Autom.*, Apr. 2005, pp. 2375–2380.

[28] A. Sadrpour, J. Jin, and A. Ulsoy, "The role of operator style on mission energy requirements for tele-operated unmanned ground vehicles," in *Proc. Amer. Control Conf.*, Jun. 2014, pp. 1553–1559.

[29] Y. Mei, Y.-H. Lu, Y. Hu, and C. Lee, "Deployment of mobile robots with energy and timing constraints," *IEEE Trans. Robot.*, vol. 22, no. 3, pp. 507–522, Jun. 2006.

[30] J. Morales, J. Martinez, A. Mandow, A. Pequeno-Boter, and A. Garcia-Cerezo, "Simplified power consumption modeling and identification for wheeled skid-steer robotic vehicles on hard horizontal ground," in *Proc. 2010 IEEE/RSJ Int. Conf. Intell. Robot. Syst.*, Oct. 2010, pp. 4769–4774.

[31] S. Dogru and L. Marques, "Power characterization of a skid-steered mobile field robot," in *Proc. 2016 Int. Conf. Auton. Robot Syst. Competitions*, May 2016, pp. 15–20.

[32] P. Millett, "Calculating motor driver power dissipation," Texas Instruments, Dallas, TX, USA, Tech. Rep. SLVA504, Feb. 2012.

[33] Electro-Craft Corporation, Ed., *DC Motors, Speed Controls, Servo Systems*, 4th ed. New York, NY, USA: Pergamon, 1972.

[34] "Understanding power MOSFET data sheet parameters," NXP Semiconductors, Eindhoven, The Netherlands, Application Note AN11158, Feb. 2014.

**Sedat Dogru** received the B.S. degree in electrical and electronics engineering, the B.S. degree in physics, and the Ph.D. degree (working on wireless sensor networks and mobile robots) in electrical and electronics engineering, all from Middle East Technical University, Ankara, Turkey, in 2000, 2001, and 2012, respectively.

He is a Postdoctoral Fellow with the Field Robotics Group, Institute of Systems and Robotics, University of Coimbra, Coimbra, Portugal. His main research interests include mobile robotics, field robotics, and computer vision.

**Lino Marques** (M'01) received the Graduate degree in 1992, the M.Sc. degree in 1997 (working on opto-electronic range sensors for robotics), and the Ph.D. degree in 2005 (working on mobile robotics olfaction), all from University of Coimbra, Coimbra, Portugal, all in electrical engineering.

He is currently a Senior Lecturer with the Department of Electrical and Computer Engineering, University of Coimbra, where he is Head of the Field Robotics Group, Institute of Systems and Robotics. He coordinated activities of ISR-UC in the FP7-TIRAMISU project, involving the research and development of robotics and sensing technologies for humanitarian demining. His main research interests include field and service robotics, robotics for environmental monitoring, cooperative and swarm robotics, mobile robot olfaction, and smart sensors.